ATMOSPHERIC SCIENCE

Upward propagation of gigantic jets revealed by 3D radio and optical mapping

Levi D. Boggs[1]*, Doug Mach[2], Eric Bruning[3], Ningyu Liu[4], Oscar A. van der Velde[5], Joan Montanyá[5], Steve Cummer[6], Kevin Palivec[7], Vanna Chmielewski[8,9], Don MacGorman[8], Michael Peterson[10]

Occasionally, lightning will exit the top of a thunderstorm and connect to the lower edge of space, forming a gigantic jet. Here, we report on observations of a negative gigantic jet that transferred an extraordinary amount of charge between the troposphere and ionosphere (~300 C). It occurred in unusual circumstances, emerging from an area of weak convection. As the discharge ascended from the cloud top, tens of very high frequency (VHF) radio sources were detected from 22 to 45 km altitude, while simultaneous optical emissions (777.4 nm OI emitted from lightning leaders) remained near cloud top (15 to 20 km altitude). This implies that the high-altitude VHF sources were produced by streamers and the streamer discharge activity can extend all the way from near cloud top to the ionosphere. The simultaneous three-dimensional radio and optical data indicate that VHF lightning networks detect emissions from streamer corona rather than the leader channel, which has broad implications to lightning physics beyond that of gigantic jets.

INTRODUCTION

Upward electrical discharges from thunderstorms can take on many different forms and characteristics. They are primarily classified by their terminal altitude in the atmosphere, ranging from brief pulses of light that are confined to altitudes near cloud top (pixies) to blue diffuse cones of light that reach approximately 40 km altitude (blue jets) to large, tree-like structures that reach all the way to the lower ionosphere (gigantic jets) (*1*–*3*). These phenomena are part of a larger family of upper atmospheric electrical discharges known as transient luminous events (TLEs). Of all the TLEs, gigantic jets are exceedingly rare (*4*) and perhaps the most spectacular, as they directly couple the lower and upper atmosphere and are capable of large charge transfers between these regions (*5*–*7*).

Most gigantic jets have been observed to emanate from maritime tropical environments, typically over the ocean and at low latitudes, during hurricane season when ocean surface temperatures are warm (August to November in the Northern Hemisphere) (*5*, *7*–*16*). The parent thunderstorms usually have tall cloud tops (15 to 18 km altitude), often overshooting into the tropopause, which is a characteristic of severe convection (*12*, *13*, *16*). The discharges commonly emerge from the convective core of the thunderstorm that is associated with the coldest cloud tops. They have also been associated with convective pulses or surges, which are defined as a period of rapid thunderstorm intensification (*12*–*14*). These convective pulses are associated with strong storm top divergence and turbulent mixing at cloud top (*13*, *14*). The cloud top turbulent conditions are thought to be a necessary prerequisite for gigantic jet production, as this weakens the upper positive charge by mixing with the upper negative screening charge layer, inducing a charge imbalance in the thunderstorm allowing the discharge to escape upward (*14*, *17*, *18*). Past observations and modeling (*14*) demonstrate that gigantic jet charge structures feature a narrow, truncated upper positive charge region over a larger, wider middle negative charge region. The narrow upper positive charge region is suggested to be a result of the turbulent mixing at cloud top. This charge structure produces an escaped negative leader that propagates vertically above the cloud and also creates a charge imbalance between the charge regions.

Similar to ordinary lightning, gigantic jets are plasmas consisting of both leaders and streamers. Lighting leaders are hot (>5000 K), highly conducting channels that excite atomic nitrogen and oxygen, with the strongest optical emissions coming from the multiplet at 777.4 nm (OI) (*19*–*22*). Streamers are filamentary, weakly ionized channels that are relatively cool (<500 K) (*23*, *24*) and produce optical emissions from molecular nitrogen (*25*), which have strong spectral lines at 337 and 427 nm from $2PN_2$ and $1NN_{2+}$. Streamers appear blue below the stratopause (<40 to 50 km altitude) due to these emission lines and the quenching of emissions with longer wavelengths (*25*). For ordinary lightning, streamer zones are located at the tips of propagating leaders, with leader channels forming the bulk structure of the discharge. For gigantic jets, the discharge begins inside the cloud as an ordinary lightning leader (with a streamer zone at the leader tip) that escapes the upper cloud charge region (*6*, *14*, *17*, *18*). The discharge transitions from a leader channel to a streamer-only mode of propagation somewhere above the cloud as it propagates to the lower ionosphere (*26*, *27*).

From most measurements of gigantic jets, there is typically a morphology change in the upward propagating discharge that occurs around 35 to 50 km altitude. Some studies have speculated, therefore, that propagation transitions from a leader mode to a streamer mode in this altitude range (*28*–*31*). The change in morphology was observed from low-speed video observations (16 to 32 ms time resolution), which showed abrupt acceleration in upward progression beginning near these altitudes. Below this altitude range, a few

[1]Severe Storms Research Center, Sensors and Electromagnetic Applications Lab, Georgia Tech Research Institute, Smyrna, GA, USA. [2]Science and Technology Institute, Universities Space Research Association, Huntsville, AL, USA. [3]Department of Geosciences, Texas Tech University, Lubbock, TX, USA. [4]Department of Physics and Space Science Center, University of New Hampshire, Durham, NH, USA. [5]Lightning Research Group, Electrical Engineering Department, Politécnica de Catalunya, Terrassa, Spain. [6]Electrical and Computer Engineering Department, Duke University, Durham, NC, USA. [7]Hawley, TX, USA. [8]Cooperative Institute for Severe and High-Impact Weather Research Operations, University of Oklahoma, Norman, OK, USA. [9]NOAA/OAR National Severe Storms Laboratory, Norman, OK, USA. [10]ISR-2, Los Alamos National Laboratory, Los Alamos, NM, USA.
*Corresponding author. Email: levi.boggs@gtri.gatech.edu

well-defined channels were observed propagating at speeds similar to those of lightning leaders (10^5 m s^{-1}). Above this range, the discharge appeared highly fanned, resembling sprites. However, van der Velde *et al.* (*27*) synthesized disagreeing evidence gleaned from the literature, suggesting that streamers may actually begin their propagation at much lower altitudes. Summarizing these points, observations show abundant filamentary structures near cloud top that have V-shaped branching (resembling laboratory streamers), discontinuities in brightness from the discharge at cloud top and above (suggestive of a leader-to-streamer transition) (*32*), and a blue color below 40 km altitude from photographs (attributable to molecular nitrogen emission by streamers).

van der Velde *et al.* (*27*) were the first to present high-speed images of gigantic jets (0.2- to 1.1-ms time resolution) and found bidirectional propagation with at least one luminous step at the altitudes of 32 to 40 km before a continuous acceleration to the ionosphere. These stepping phenomena did not have the classical signs of a stepped leader, and the authors of that study suggested it may be a form of "pilot streamer" propagation, which is observed in laboratories for negative streamers (*33*–*35*). While the high-speed images suggest a stepped form of streamer propagation before the final upward extension to the ionosphere, the lower portion (<32 km altitude) of the discharge was not observed because of atmospheric scattering and camera sensitivity. Hence, measurements of the lower portion of gigantic jets would be greatly beneficial in understanding the discharge physics in this region.

Here, we report on a gigantic jet that transferred an extraordinary amount of charge (~300 C) to the ionosphere and discharged a huge area (~60 km by 60 km) of the thundercloud. The charge transfer is nearly double the previous largest by a gigantic jet (*5*) and is comparable to the largest ever recorded for cloud-to-ground strokes (*36*, *37*). The event occurred in unusual circumstances, with the parent storm cell characterized by relatively warm cloud tops and an absence of turbulent mixing. The event took place very close to the center of a radio [very high frequency (VHF)] lightning mapping array, which provided unprecedented three-dimensional (3D) VHF data that mapped the discharge both inside and above the cloud, up to 45 km altitude. Through new data processing techniques using the Geostationary Lightning Mapper (GLM) 16 and 17 observations, optical emissions from the multiplet at 777.4 nm (OI) are mapped in three dimensions (latitude, longitude, and altitude) for this event (*38*). The combined 3D radio and optical data provide key insight into the plasma nature of gigantic jets. In addition, the radio and optical data show the first clear evidence that the VHF observed by lightning networks is produced by streamers ahead of the leader.

RESULTS

Thunderstorm environment

The gigantic jet occurred on 14 May 2018 in southwest Oklahoma and was recorded with a low-light level Watec camera located to the south in Hawley, Texas (see movie S1). The parent storm system that produced the gigantic jet was unusual compared to most gigantic jet-producing systems (*7*–*10*, *15*), as it developed during the Northern Hemisphere spring, was not associated with a tropical environment, and was located at relatively high latitudes (approximately 35°N). Figure 1A shows the Geostationary Operational Environment Satellite (GOES) infrared (IR) channel 13 cloud top brightness temperature for the convective region near the gigantic jet. The gigantic jet was located around 35.0°N, 99.5°W, in a region of uniform and relatively warm cloud top temperature (210 K). This location was far displaced from the coldest cloud tops (near 195 K), which were located approximately 100 km to the southwest (34.5°N, 100.8°W). Figure 1B shows the radar structure at mid-levels (6 km altitude) associated with Fig. 1A (bounded by the black box). The coldest cloud tops were dominated by large reflectivity values (40 to 55 dBZ) from intense convective cores, while the gigantic jet occurred in a region of much lower reflectivity (15 to 30 dBZ) that is a characteristic of stratiform precipitation. The total lightning density (flashes per 2 km by 2 km bin) from the National Lightning Detection Network (*39*) for a 10-min period around the time of the gigantic jet is shown in Fig. 1C. The convective region that produced the gigantic jet was associated with low lightning density during this period, reflective of the weak stratiform convection in this region. This is heavily contrasted with the large lightning densities that occurred to the southwest that were associated with the coldest cloud tops and large reflectivity values from Fig. 1 (A and B).

To demonstrate the unique characteristics of the parent storm that produced the gigantic jet in Fig. 1, its thunderstorm properties are shown in Table 1 and compared with past negative gigantic jet-producing storms. These past storms were chosen as they occurred relatively close to NEXRAD (Next Generation Weather Radar) locations. The radar properties listed are the maximum value of vertically integrated liquid (VIL), the radial velocity differential (RV delta) at storm top, and the maximum value of spectrum width (Max SW) at storm top. VIL is the integration of radar reflectivity in a column of air (*40*) and can be used to classify different thunderstorm regions and locate hail. The radial velocity differential is a measure of divergence at storm top (*13*, *14*). The maximum spectrum width value is a measure of turbulence at storm top (*14*, *41*). These radar properties were taken at the location from which the gigantic jet emerged. The maximum VIL values of past negative gigantic jet-producing storms varies from 14 to 20 kg m^{-2}, while the case presented here is less than half of that with a value of 6 kg m^{-2}. This low value classifies this region as stratiform precipitation (*42*, *43*), even with the relatively intense cell that initiated the gigantic jet (discussed in the "Charge structure and event formation" section). The storm top divergence and maximum spectrum width vary from 26 to 55 m s^{-1} and 7 to 11 m s^{-1} for past gigantic jet cases, while this case exhibited no storm top divergence (RV delta = 0 m s^{-1}) and minimal storm top turbulence (Max SW = 2 m s^{-1}). The total flash rate leading up to each gigantic jet (approximately 5 min prior) is shown in the last column. Past gigantic jet cases have values of 2 to 10 flashes/min, and this case has 0. This is because the gigantic jet was the first flash that occurred in this region as it developed. The properties listed above indicate that this gigantic jet-producing region had a much weaker updraft, had little to no storm top mixing and divergence, and had no prior flashes. These are all departures from past documented regions that have produced negative gigantic jets.

Charge structure and event formation

The thunderstorm charge structure derived from VHF lightning mapping array data (for the parent flash of the gigantic jet) is overlaid on radar reflectivity of the parent storm (Fig. 2). The lightning mapping array detects and maps VHF emissions in 3D space and also time (*44*). This event was observed by two clusters of lightning mapping array sensors in Oklahoma, USA operating semi-independently

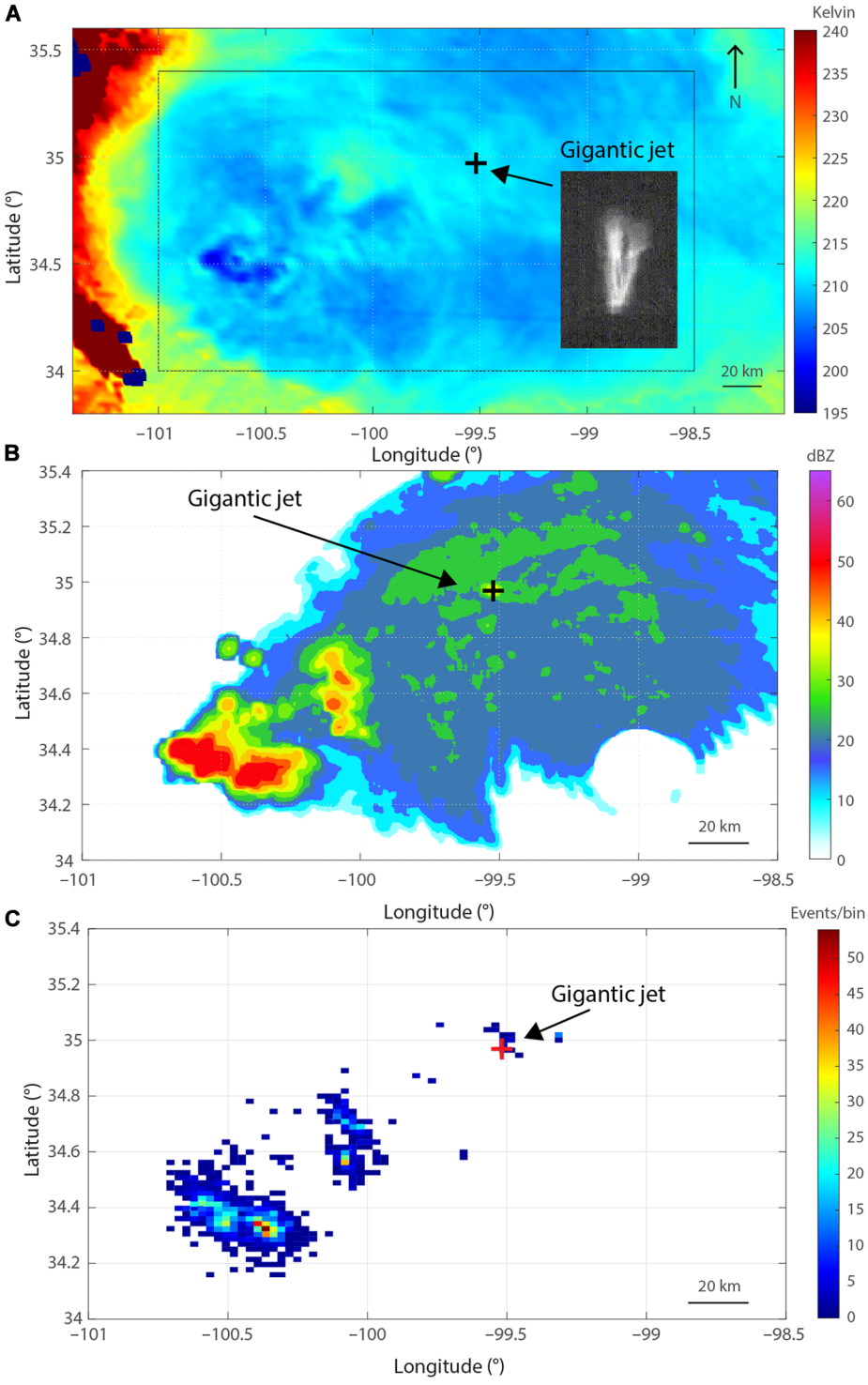

Fig. 1. Satellite, radar, and lightning data of the thunderstorm environment. (**A**) GOES Advanced Baseline Imager channel 13 (IR) brightness temperature, (**B**) NEXRAD (Next Generation Weather Radar) reflectivity [KFDR, 02:24 universal time (UT)], and (**C**) National Lightning Detection Network total lightning density of the convective environment associated with the gigantic jet. The bin size for (C) is 2 km by 2 km, and the interval is ±5 min around time of the event. The gigantic jet is denoted by a cross in each panel, with a video frame of the fully developed jet shown in (A). N, north.

Table 1. Summary of thunderstorm properties from past negative gigantic jets and this study. The flash rate is calculated for the time period approximately 5 min before each gigantic jet from National Lightning Detection Network and/or the Global Lightning Dataset (GLD360). These parameters are calculated for the thunderstorm cell that produced each gigantic jet. Max VIL, maximum vertically integrated liquid (VIL); RV delta, absolute value of outbound radial velocity minus inbound radial velocity at storm top; Max SW, maximum spectrum width at storm top. NA, not applicable.

Date (mm/dd/yyyy)	Time (UT)	Location	Max VIL (kg/m^2)	RV delta (m/s)	Max SW (m/s)	Flash rate (min)
14 May 2018 (this study)	**02:24**	**Southwest OK, USA**	**6.1**	**0**	**2**	**0**
21 July 2008 (*5*)	03:10	NC coast, USA	20.1	NA	8.5	NA
08 May 2009 (*12*)	08:08	NC coast, USA	21.6	49	7	2
09 September 2010 (*6*, *12*, *14*)	07:22	South OK, USA	14.1	38	11	10
28 September 2010 (*6*, *12*, *14*)	11:01	Northeast FL, USA	19.6	35	10	5
22 September 2011 (*12*)	05:27	Central PR, USA	17.1	26	11	2
03 August 2013 (*7*, *13*, *14*)	04:11	Southeast FL, USA	20.6	55	9	3
12 September 2014 (*14*)	06:59	South FL, USA	14.1	26	11	5

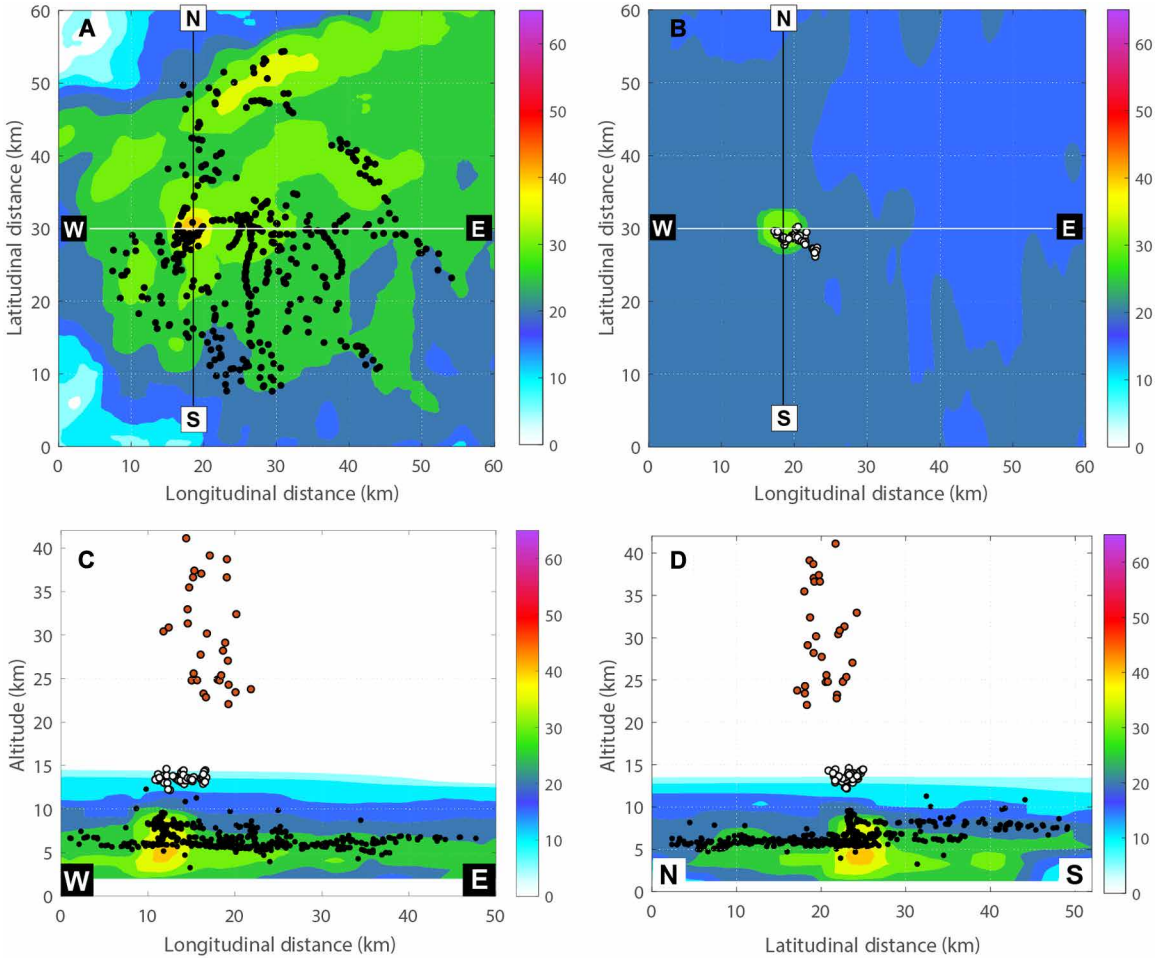

Fig. 2. Thunderstorm charge structure observed from VHF and radar data. VHF inferred (**A**) middle negative charge region (black dots) overlaid on radar reflectivity (KFDR, 02:24 UT) at mid-levels (4 to 5 km altitude) of the storm and (**B**) upper positive charge region (white dots) overlaid on radar reflectivity (KFDR, 02:24 UT) at upper levels (9 to 10 km altitude) of the storm. The white and black lines denote where the west-east (**C**) and north-south (**D**) vertical cross sections are located, respectively. The orange dots in (C) and (D) are the VHF points from the gigantic jet as it ascends to the ionosphere. W, west; E, east; N, north; S, south.

and occurred in very close proximity to one of the clusters, allowing the discharge to be mapped in detail (also see fig. S5 for an additional mapping projection). The electrical structure of the parent storm was characterized by a very wide, horizontally expansive middle negative charge region (Fig. 2A, black dots) and a localized, narrow upper positive charge region (Fig. 2B, white dots). The upper positive over middle negative charge structure is consistent with the event being of negative polarity, meaning the negative charge was transferred upward to the ionosphere (*6*, *14*, *17*). Sferics from extremely low frequency (ELF) radio data support this (fig. S4). The extreme difference in spatial extent between the two charge regions is reflected by the volume occupied by the VHF emissions in each region. The volume covered by the middle negative region is approximately 900 km^3, while the upper positive region covers about 15 km^3. This large spatial extent of the VHF emissions in the middle negative region is comparable to cloud-to-ground flashes of positive sprite-parent lightning (*37*, *45*–*47*).

While the charge densities in each region likely vary, the huge geometrical mismatch between the participating charge regions results in a charge imbalance between them of at least one order of magnitude (assuming similar charge densities). The difference in the charge regions is easily observed from the vertical cross sections in Fig. 2 (C and D). The horizontal extent of the upper positive charge region spans about 3 to 6 km compared with approximately 50 km for the middle negative charge region. The upper positive charge region is located above a small, localized convective cell that initiated the gigantic jet, shown by the yellow/orange color in Fig. 2 (C and D). The horizontal extent of this cell is similar to that of the upper positive charge region, as clearly shown in Fig. 2B (the cell is colored green, and the upper positive charge is depicted by white VHF points). The VHF emissions above the cloud associated with the gigantic jet (22 to 4 km altitude, orange points) occur above the localized convective cell (Fig. 2, C and D). The narrow upper positive charge region over a wide middle negative charge region supports the previous work on gigantic jet charge structures (*14*) but on a much more drastic scale. The huge size difference, and presumed charge difference, between the charge regions also clearly demonstrates the role of charge imbalance in gigantic jet formation previously stated in prior studies (*14*, *17*, *18*).

Figure 3 shows the time evolution of the small convective cell that initiated the gigantic jet. The panels show a 3D surface of radar reflectivity at 30 dBZ, which captures the evolution of this cell as it developed to produce the event. The gray horizontal planes represent the radar echo cloud top. Approximately 15 min before gigantic jet initiation, the 30-dBZ surface is stratified near 5 km altitude (Fig. 3A). From the next radar volume scan (about 5 min later), a small, convective perturbation begins to form (indicated by the arrow in Fig. 3B). The altitude of this perturbation is 6.5 km at this time. Subsequently, the convective perturbation starts to intensify, forming a vertical convective cell (Fig. 3C) and reaching an altitude of 8.2 km. The gigantic jet occurs during the next volume scan, emerging from the location of the localized convective cell (Fig. 3D), which has reached 8.7 km altitude. The VHF lightning mapping array data show the flash emanate from the convective cell (black dots), propagate into the narrow upper positive region (white dots), and then extend upward well above cloud top to 40 km altitude (orange dots). The upper positive charge has a similar lateral extent as the initiating convective cell, suggesting the convective cell–lofted positive charge near cloud top that initiated the event. Although that region of the convective cell developed quickly and is more intense than the surrounding stratified region, it did not exhibit any storm top divergence signatures or turbulent mixing near cloud top, as evidenced by the radial velocity differential and spectrum width listed in Table 1 (also see figs. S2 and S3).

Simultaneous radio and optical measurements

In addition to the VHF lightning mapping array, the gigantic jet flash was simultaneously observed by ground-based low-frequency magnetic field sensors (*5*, *27*) and the GLM on GOES 16 and 17 (*15*, *48*). This allowed a detailed look into the electrical structure of the event. GLM detects the 777.4-nm (OI) multiplet from hot lightning leaders and return strokes (*22*, *49*–*52*) and maps the emissions in 2D (latitude and longitude) space and time. However, our analysis used a new technique to estimate the altitude of GLM emissions, in addition to the traditional latitude and longitude, which was made possible by simultaneous observations (i.e., stereo) from both GLMs (see details in Materials and Methods) (*38*). A similar technique has been used to calculate the altitude of bolides high in the atmosphere (tens of kilometers in altitude) from stereo GLM observations (*53*). The magnetic field data allowed the current moment and charge moment change to be calculated from recorded waveforms.

The discharge began as a normal, bilevel intracloud flash between the upper positive and middle negative charge region (dark blue points in Fig. 4). During this time, optical (777.4 nm OI) emissions occurred near cloud top (gray diamonds), associated with the negative leader in the upper positive charge region. The discharge then escaped upward from the upper charge region (15 to 17 km altitude and 0.35 s in Fig. 4, A and B). Subsequently, there was a gap in VHF and optical emissions above cloud top, until approximately 0.45 s after the start of the flash. However, during this time (0.35 to 0.45 s), there was prolific VHF activity at 6 to 8 km altitude from emissions associated with the positive leader network inside the middle negative charge region. The next VHF emissions began around 22 km altitude and continued until approximately 45 km altitude. These emissions occurred as the gigantic jet propagated upward to the ionosphere, with ionospheric connection occurring approximately 0.5 s after the start of the flash (vertical blue line; Fig. 4, A and B). During the VHF activity above the cloud, the optical emissions remained just above cloud top (black diamonds), well below the altitudes of the VHF sources. After the ionospheric connection, the optical emissions gradually increased in altitude. Similar behavior has been observed in ground-based images of gigantic jets that show the bright base of the jet increase in altitude during the trailing jet phase (fig. S1) (*7*, *8*, *15*, *27*). Subsequently, the VHF activity in the middle negative charge region persisted for another second, extending radially outward. Figure 4 (C and D) shows that the optical (777.4 nm OI) emissions are mapped to the base of the gigantic jet, predominantly above cloud top but below the VHF activity at 22 to 45 km altitude. When comparing with the VHF activity alone (Fig. 4, C and D, insets), the optical emissions show a single branch structure and trace out a path between the VHF activity at cloud top and the VHF activity above 22 km altitude. The VHF activity above 22 km has a much wider horizontal extent and is less compact than the optical emissions above the cloud.

The VHF power, optical energy, and current moment indicating negative charge moving upward are shown for the parent flash and the ascending gigantic jet in Fig. 5. Before the discharge exited the upper charge region (i.e., before roughly 0.3 s), most of VHF emissions came from the middle negative charge region and were associated

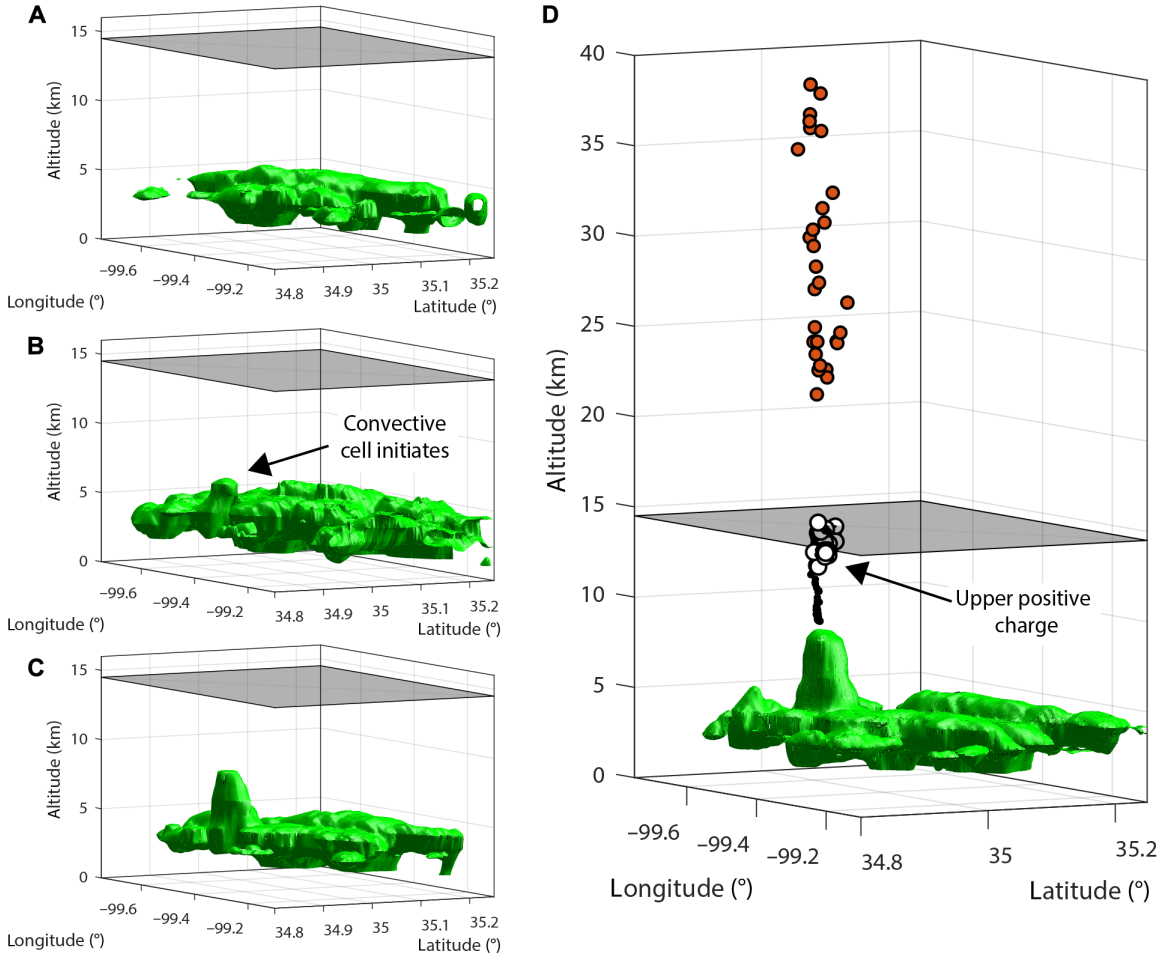

Fig. 3. Evolution of the convective region that produced the gigantic jet. The 3D surface (green) represents the 30-dBZ radar echo for four consecutive volume scans from the KFDR radar (Frederick, OK, USA). The start time for each volume scan is (**A**) 02:10 UT, (**B**) 02:15 UT, (**C**) 02:20 UT, and (**D**) 02:24 UT. In (D), the black dots are the VHF emissions from the initial upward escape, the white dots represent the upper positive charge region (indicated by an arrow), and the orange dots are from the discharge as it ascends toward the ionosphere. The gray plane represents the radar echo cloud top.

with the network of positive leaders propagating through that region (mostly within the 5 to 8 km altitude). Subsequently, the upward negative leader escaped (between 0.32 and 0.35 s in Fig. 5A) near the end of a lull in the VHF activity in the middle negative charge region. The escaping negative leader produced emissions whose VHF power ranged from 4 to 14 dBW and whose optical energy ranged from 2 to 164 fJ (VHF power and optical energy magnitudes are shown in Fig. 5A by the size of the red dots and gray diamonds, respectively).

After the initial upward escape (between 0.32 and 0.35 s in Fig. 5A), there was a gap of almost 100 ms in the VHF and optical emissions above 8 km. Close inspection of the VHF data suggests that this gap is real. Although it is possible that the prolific VHF emissions in the midlevel negative charge occurred close enough in time to high-altitude VHF emissions to interfere with their detection, the rate of received VHF emissions was much less than the rate at which the lightning mapping array (LMA) can process them (see figs. S10 and S11). Thus, it is likely that at least some high-altitude VHF emissions would have been detected if they had occurred. The fact that optical and VHF emissions were not detected above 8 km during the gap and that current moment changes were small (Fig. 5B and fig. S4) strongly suggest that the discharge was static (i.e., had no upward progression). The resumption of VHF and optical emissions near and above cloud top occurred at approximately the time VHF activity in the middle negative charge region became less active (Fig. 5A). The high-altitude discharge depicted by VHF emissions began to accelerate upward, from speeds on the order of 10^5 m s^{-1} at 22 to 26 km altitude to speeds of 10^6 m s^{-1} above 26 km. These velocities were obtained from a smooth exponential line fitted to the VHF points, but the points occurred intermittently (Fig. 5B), with a mean time between sequential points of 4.7 ms. Some of the intermittent changes in altitude could possibly be interpreted as being consistent with stepwise progression for the VHF activity above the cloud.

A detailed look at the period following the resumption of VHF and optical emissions (Fig. 5B) shows the VHF power of points above cloud top increased with increasing altitude, ranging from 1 to 21 dBW and peaking at an altitude of nearly 45 km. The current moment of the gigantic jet also began to increase during this period, although with undulations. The undulations in current moment may be further evidence that the gigantic jet discharge propagated upward in steps above the cloud top. When the velocity of upward

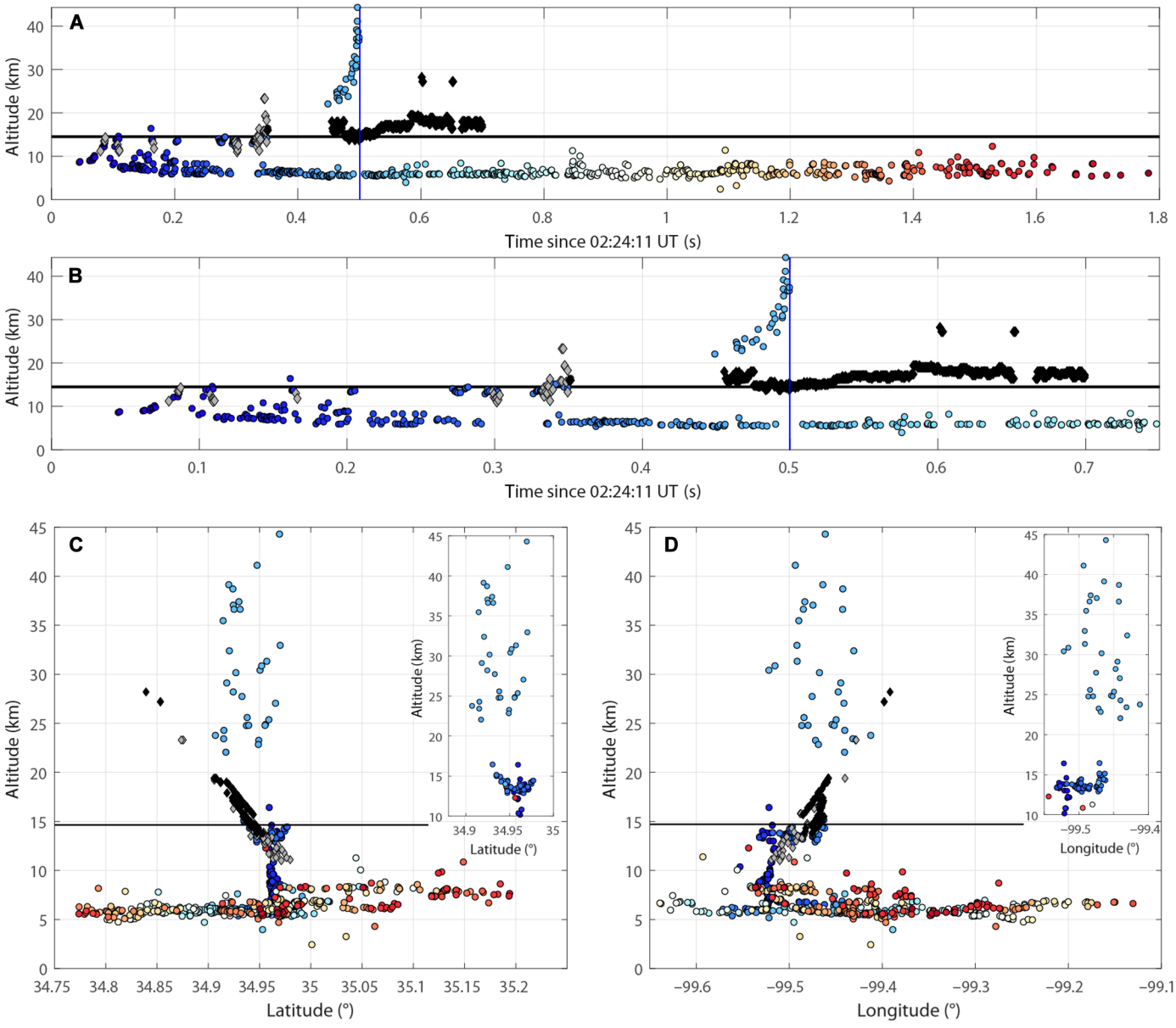

Fig. 4. Comparison of VHF and optical (777.4-nm OI) data of the gigantic jet. (**A**) Time versus altitude plot of VHF and optical (777.4-nm OI) emissions of the entire parent flash. The VHF data (circles) are colored according to time and the optical data (diamonds) are either gray (associated with in-cloud VHF activity) or black (associated with above-cloud VHF activity). (**B**) Zoomed plot of (A). Latitude (**C**) and longitude (**D**) versus altitude plots of the VHF and optical emissions. Each panel inset in (C) and (D) shows the VHF emissions only for reference. The black horizontal line represents the radar echo cloud top in each panel. The vertical blue line in (A) and (B) represents when the discharge connected to the ionosphere.

propagation of VHF emissions increased to approximately 10^6 m s^{-1}, the current moment also increased rapidly to a peak value of 160 kA/km. The optical emissions in Fig. 5B increase in optical energy from 3 to 60 fJ (shown by the size of the black diamonds) until approximately the time of the ionospheric connection (gray shaded region in Fig. 5B, from 0.495 to 0.501 s), where they peak at 180 fJ.

DISCUSSION

The behavior of the discharge above the cloud after the initial escape of the leader from the cloud may be explained by the associated in-cloud flash activity and thunderstorm charge structure. Figure 6A shows the charge structure leading to the escaped negative leader, found by the volume bounding the VHF points in each region. Up to the time of escape, the upper positive and middle negative charge were similar in size, with volumes of 15 and 17 km^3, respectively (Table 2). If the VHF source density is used as a proxy for storm charge density (*17*, *54*–*57*), then the middle negative charge region had an approximately 50% larger charge density.

We infer from the prolonged gap in VHF sources above cloud top between approximately 0.35 and 0.45 s in Fig. 5A that the negative leader stopped propagating upward right after it first escaped

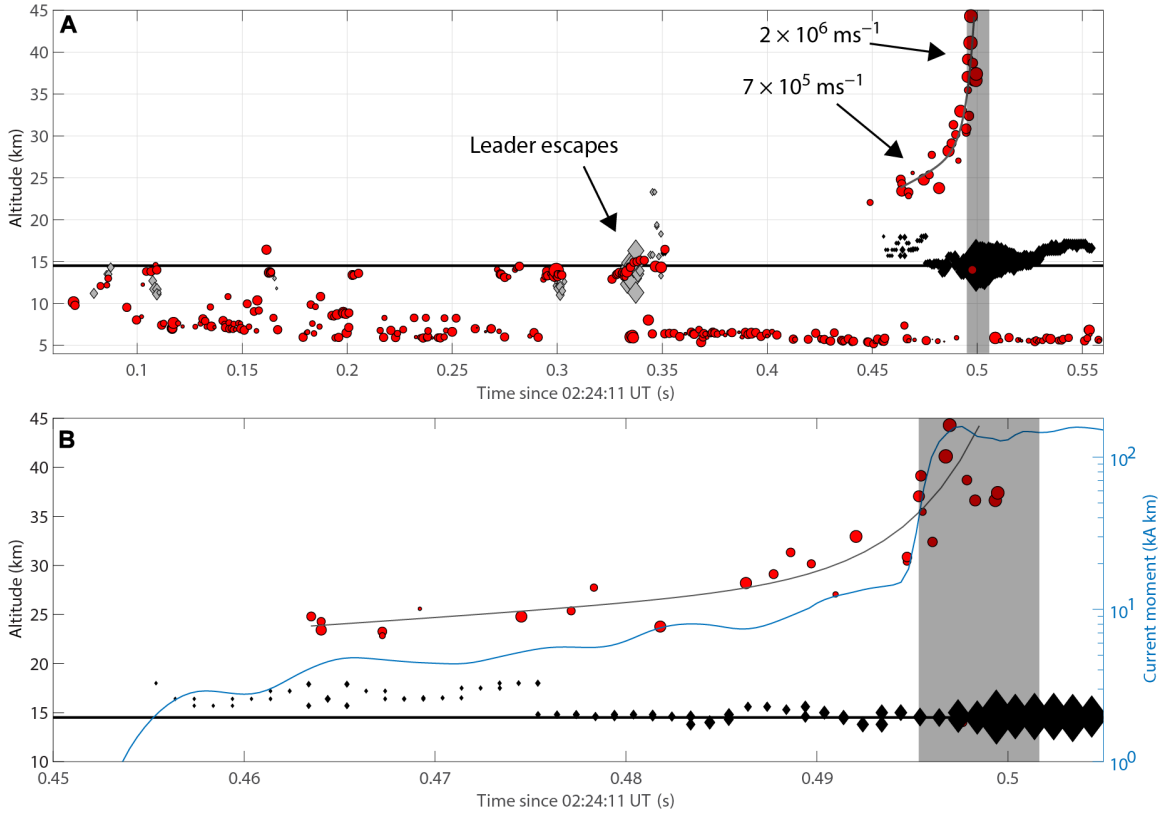

Fig. 5. VHF power, optical (777.4-nm OI) energy, and current moment of the ascending gigantic jet. (**A**) Time versus altitude plot of the VHF and optical (777.4-nm OI) emissions. The VHF data (circles) are colored red and the optical data (diamonds) are either gray (associated with in-cloud VHF activity) or black (associated with above-cloud VHF activity). The VHF and optical data vary size according to VHF power and optical energy, respectively. (**B**) Zoomed region of (A) when the discharge was accelerating upward with current moment overlaid (blue). The horizontal black line in (A) and (B) represents the radar echo cloud top, and the vertical gray bar represents when the discharge connected to the ionosphere. The solid gray line represents an exponential fit to the VHF data.

the cloud. During this gap, the network of positive leaders propagating through mid-level negative charge expanded considerably, nearly doubling in volume (Fig. 6B and Table 2). After the gap, the upward current surged, and the altitude of VHF sources rose from 22 to 45 km as the discharge accelerated to the ionosphere (Fig. 5). Once the gigantic jet reached the ionosphere, the mid-level positive leader network expanded horizontally inside the extensive negative charge layer for more than a second (Fig. 6C and Table 2), thereby producing the incredible charge transfer associated with this event, although we infer that the portion of the negative layer now tapped had a smaller charge density than the portion that initiated the flash (Figs. 4 and 5and Table 2).

This evolution suggests that the larger inferred charge density and slightly larger volume of the middle negative region imparted a negative potential to the upward leader network, allowing the negative leader to escape the cloud. However, the two charge regions were similarly sized, so the potential difference between them could well have been insufficient to drive the leader propagation more than a few kilometers above the cloud top. During the gap in high-altitude VHF sources, the potential of the leader network shifted to a much more negative value as the positive leader network expanded through the middle negative charge region. Once the potential was sufficiently negative, the discharge propagated upward, producing the VHF sources above 20 km altitude. This suggests that had the positive leader network not been able to expand farther into the middle negative charge region after the negative leader initially escaped, the discharge would have ceased propagating together and would resemble a starter, which reaches only a couple kilometers above the cloud top. A negative starter was observed above tropical storm Dorian that also produced gigantic jets, and Liu *et al.* (*7*) speculated a similar explanation for the occurrence of the starter. This evolution shows the importance of having an expansive middle negative charge region to form gigantic jets and suggests that the terminal altitude of upward discharges is linked to the thunderstorm charge structure.

The incredibly large charge moment change (22,000 C/km), current moment (160 kA/km), and charge transfer (293 C assuming 75 km channel length) for this event appear to be a consequence of the unique thunderstorm charge structure that produced it. A similar charge structure that features narrow upper positive over wider middle negative charge has been formulated for gigantic jets from a prior study (*6*, *14*), but the charge structure presented here is an extreme version of that. Furthermore, the formation mechanisms of the previously formulated charge structure and this one are very different. Past gigantic jet thunderstorms show large storm top divergence and heavy cloud top turbulence (*13*, *14*, *16*) associated with an overshooting cloud top, which is consistent with the hypothesis that the upper negative screening layer is being folded and mixed into the upper positive charge region. The divergence pushes the screening charge away from the central axis of the updraft, and spatial patterns in turbulent regions suggest that it is mixed outside a

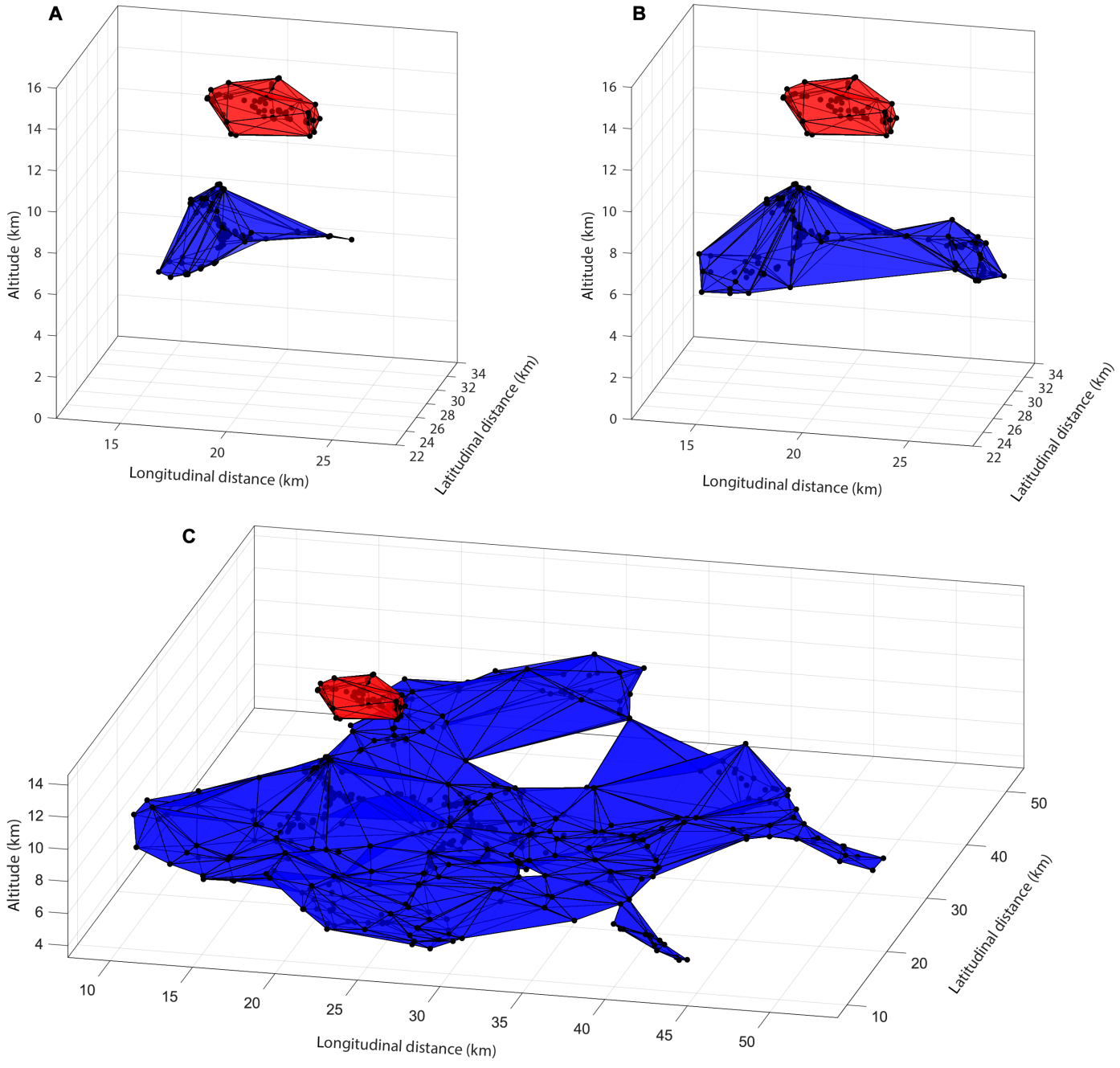

Fig. 6. Charge regions bounding the VHF data as a function of time. (**A**) MN_1 from Table 2, (**B**) MN_2, and (**C**) MN_3. The blue volume represents the middle negative charge and the red volume represents the upper positive charge. Note that the volumes show the cumulative extent of the middle negative charge region in each panel, whereas Table 2 shows the difference in volume between time periods.

relatively narrow updraft (*14*). This results in a truncated upper positive charge region with respect to the middle negative charge region and a charge imbalance between them.

However, this study shows that a charge distribution having a local imbalance in charge polarity, with an excess of middle negative charge, can be produced in a different way without substantial storm top divergence, local mixing of screening-layer charge, or an overshooting cloud top. Figure 3 indicates that the upper positive charge was lofted to high altitudes by a convective perturbation. Because the perturbation was small and localized, so was the upper positive charge region associated with it. Support for this interpretation is provided by the horizontal extent of the upward progression of VHF emissions near cloud top, which presumably reflects the horizontal extent of the upper positive charge region, being similar to the horizontal extent of the convective perturbation indicated by a rising 30-dBZ radar echo beneath them (Figs. 2B and 3D). The positive and negative charges created by this small perturbation were superposed on the vast, stratified middle negative charge of the overall

Table 2. Statistics describing the charge regions as a function of time. For MN_1 to MN_3, the volume is not cumulative and corresponds to only the volume occupied during the time interval in the last row. MN_1 corresponds to the initial flash just before the escaped leader, MN_2 is after the escaped leader but before the high-altitude VHF is emitted, and MN_3 is after the high-altitude VHF is emitted. UP, upper positive; MN, middle negative.

	UP	MN_1	MN_2	MN_3	MN_{total}
Volume (km^3)	14.9	17	29.5	837.2	883.7
VHF source density ($sources/km^3$)	3.8	5.9	2.4	0.5	0.7
Seconds after 02:24:11 UT	0–0.35	0–0.29	0.33–0.46	0.46–1.78	0–1.78

storm system down-shear of the distant deep convection. Thus, the requisite charge structure was achieved in a region without a convective cell vigorous enough to be apparent in storm top divergence and turbulent mixing. Our data do not allow us to assess how the vast negative charge region was formed. Down-shear advection of negatively charged ice crystals from thunderstorm cores near the Oklahoma/Texas border would require an inverted electrical structure (*58*). In situ electrification in a weak mesoscale updraft is also possible (*59*). The presence of vertical wind shear can also cause differential advection of charge, so it is possible that any upper positive charge in this region could have been advected southward, leaving a sheared-off region of middle negative charge. Extensive flashes occurred in an upper positive charge region south of the gigantic jet a few minutes after the event, supporting this scenario. The relative speed differential between upper levels (>9 km altitude) and lower levels (<9 km altitude) was 30 m s^{-1}, with the upper level winds blowing southward and lower level winds blowing northward. Similar wind shear was reported for an unusual wintertime gigantic jet (*60*).

This study provides further evidence that the charge structure from which negative gigantic jets develop is relatively simple, dipolar in nature, with mismatched sizes of upper positive and middle negative charge. There was no evidence of a lower positive charge center, as there were no low-altitude VHF sources below the negative charge and there were no cloud-to-ground strikes until about 4 min after the gigantic jet. This lack of cloud-to-ground strikes allowed a large enough excess of negative charge to accumulate at middle altitudes, so that, when a flash did occur, it initiated the gigantic jet.

Unlike the previously documented cases noted in Table 1, this gigantic jet occurred more than 50 km from deep convection and even farther from the vigorous convection associated with the coldest cloud tops in Fig. 1. Although these vigorous cells exhibited values of spectrum width (10 to 13 m s^{-1}) and radial velocity differentials (20 to 25 m s^{-1}) at cloud top that were comparable to those of the previous gigantic jet cases, their flash rate (80 per minute) was much larger (Table 1) (*7*, *12*–*14*). This large flash rate consisted of many small flashes (see movie S2), due to the frequent formation and discharge of many small pockets of charge around the strong updraft, which would not allow a large region of excess negative charge to form in the cell. Thus, having cloud-top properties similar to those of previously observed gigantic jets is not sufficient; the underlying electrical structure of the cell is critical. Furthermore, the gigantic jet reported here occurred where cloud-top conditions indicated much weaker convection than in previous cases; it appeared to occur in relatively weak convection, several tens of kilometers from deep convection. We conclude that the mismatched dipolar charge structure described above, however it may be achieved, is likely what drives negative gigantic jets and can be produced from different environments and from different storm processes.

The simultaneous VHF and optical (777.4 nm OI) emissions provide key information about the electrical structure and propagation of the gigantic jet. As the discharge initially escaped upward, it had relatively large optical energy and the VHF power was relatively small (0.32 to 0.35 s; Fig. 5). Later, when the discharge began propagating to the ionosphere, the VHF power at upper altitudes (22 to 45 km) was larger but there were no associated 777.4-nm (OI) emissions at these altitudes; they were confined to near cloud top. If the leader had reached 22 to 45 km, where the high VHF emissions were produced, then the higher temperature characteristic of leaders likely would have been associated with optical pulses that radiate at 777.4 nm (OI) (*20*, *22*, *49*, *52*). The lack of these optical emissions suggests that the VHF emissions produced at 22 to 45 km were not from a hot leader discharge but from streamers, which are cooler. Considering that the leader was constrained to low altitudes (15 to 20 km), this indicates that streamers are capable of extending all the way to the lower ionosphere from near cloud top.

One consequence is that the lower portion of the discharge above the cloud should appear blue, the color of streamers at that altitude, similar to blue jets (*2*, *25*, *61*), due to the emissions of molecular nitrogen and the quenching of longer wavelengths in the stratosphere. Recent rare color video footage of a gigantic jet captured from an airliner at 35,000 feet (10.7 km) altitude shows that it is predominantly blue from cloud top to higher altitudes, with bright white color only at the base near cloud top (fig. S1). Other observations with color footage of gigantic jets have a similar appearance (*10*, *31*, *62*). The bright white portion is the leader channel that climbs higher in altitude after the ionospheric connection, and the optical (777.4-nm OI) emissions plotted in Figs. 4 and 5 show a similar evolution. This has also been observed for other cases (*6*–*8*, *10*, *15*, *27*). Furthermore, the spatial structure shown in Fig. 4 (C and D) shows strong contrast between the VHF emissions from 22 to 45 km altitude and the optical (777.4-nm OI) emissions. The VHF emissions have an outward, wide, chaotic appearance, while the optical emissions are confined locally in space between cloud top and the VHF emissions at high altitudes. This appearance is similar to close ground-based footage of gigantic jets that show a bright, singular channel right above cloud top with much dimmer, outward protruding filaments above it (*6*, *7*, *15*).

The exponential evolution of the rise of VHF sources above the cloud (Fig. 5) appears similar to the evolution seen in optical recordings of the leading jet from low frame rate cameras. Figure 1 of da Silva and Pasko (*30*) shows two examples with an initial constant upward speed followed by vertical acceleration. Past modeling studies

have attributed this acceleration to the expansion of the streamer zone of the ascending leader (*30*, *63*–*65*), which is itself due to the exponential decrease with altitude in atmospheric neutral density. Figure S7 (top) shows the VHF sources above the cloud overlaid with the atmospheric neutral density from the MSIS-E-90 atmospheric model (*66*). While the vertical progression of VHF sources is not smooth and follows a sawtooth pattern, the smoothed trend is roughly exponential and is similar to that of atmospheric density. Because these VHF emissions were produced by streamers, as discussed above, the vertical acceleration appears to be related to the expansion of the streamer zone as proposed by previous modeling studies (*63*, *64*). However, the sawtooth pattern in the vertical progression of VHF sources may suggest a discontinuous, step-like mode of propagation, rather than a continuous extension of the streamer zone.

Furthermore, the study of high-speed video by van der Velde *et al.* (*27*) showed that the gigantic jets they observed exhibited bidirectional stepwise evolution at altitudes of 32 to 40 km before the final extension to the ionosphere. For the events in that study, there were no optical pulses resembling stepped leaders (as opposed to streamers) and the current density was significantly lower (by five to six orders of magnitude) during the trailing jet than would be expected of leaders. The authors of that study suggested a morphology similar to that of negative streamers observed in laboratories, which can undergo a pilot system of propagation. In this mode of propagation, the streamers evolve in a stepwise bipolar fashion, with space stems forming that emit forward extending negative streamers and backward extending positive streamers (*33*–*35*). The backward extending positive streamers connect with the initial negative streamers (emitted from the high-voltage electrode), forming a quasi-stationary streamer channel [termed secondary streamer or preleader (*33*)], and this process repeats until the streamer system reaches the other electrode. It should be noted that the pilot system for stepped leaders of cloud-to-ground flashes is similar, but, in that case, the space stem and stationary streamer channel transform into space leaders and leader channels as the temperature increases to a point at which the detachment of negative ions markedly increases the channel conductivity (*35*).

The VHF produced by the gigantic jet at 22 to 45 km altitude may support this mode of propagation and be consistent with the steps observed in the high-speed imagery of van der Velde *et al.* (*27*). For example, the VHF emissions occurred in bursts separated by approximately 8 to 12 ms in time and 2 to 6 km in altitude compared with approximately 5 to 10 ms and 2 to 5 km, respectively, in the high-speed imagery. Furthermore, the current in the jet shows considerable variation, with approximately the same number of local peaks as of VHF bursts (fig. S8, top). Similar behavior is observed in laboratory streamers, which show a variation in current associated with each streamer corona burst (*33*).

If this streamer pilot system or some similar process is taking place in gigantic jets, it is likely that the VHF emissions from 22 to 45 km altitude were produced from a collision of opposite polarity streamers. A recent modeling study has demonstrated that colliding streamers of opposite polarity produce high-frequency radiation (tens to hundreds of GHz) at ground level (*67*). When scaled to jet altitudes (25 to 45 km), the radiation shifts to lower frequencies (tens to hundreds of MHz) that are within the range typically detected by VHF lightning mapping arrays (60 to 66 MHz). However, the emissions from purely propagating streamers (i.e., no collisions) do not radiate at frequencies greater than a few MHz when scaled to jet altitudes (*67*).

Our 3D VHF and optical data suggest that VHF lightning mapping networks detect emissions from streamers, not from leader channels. We suggest that the reason the 3D optical and VHF sources we observed within the storm were emitted at essentially the same points in space and time (0.0 to 0.35 s; Fig. 4, A and B) was because the streamer zone likely was small enough to be difficult to distinguish from the leader tip at the atmospheric densities in and near the cloud. However, as the discharge propagated upward into regions with smaller atmospheric densities, the 3D optical and VHF sources were temporally coincident but spatially separated above the cloud (0.45 to 0.5 s; Fig. 4, A and B). Because the 3D optical emissions (777.4 nm OI) mapped the location of the leader channel in 3D space, and the 3D VHF emissions were tens of km above the leader indicates that the VHF emissions (detected by the LMA) were not from the leader channel but from the associated streamer corona. This has broad implications to research that uses VHF lightning mapping arrays or interferometers to study lightning physics.

In summary, we have presented observations of a negative gigantic jet that was simultaneously mapped in 3D space and time from radio (VHF) and optical (777.4 nm OI) instruments. The radio and optical data show that, as the discharge exited the cloud and propagated upward toward the lower ionosphere, the leader remained near cloud top (within a few kilometers), while streamers propagated upward to the lower ionosphere. The decoupled leader and streamer source altitudes of the ascending discharge indicate that VHF emissions detected from lightning mapping networks are produced by streamers rather than leaders. The event formed in a thunderstorm environment much different from the paradigm established by previous studies of gigantic jets, which were observed in maritime tropical storms, in the vicinity of overshooting cloud tops associated with updrafts having upper-level divergence and turbulence. Instead, the event documented here occurred several tens of kilometers from the nearest deep convection and overshooting tops. The charge structure that produced the gigantic jet consisted of a relatively compact positive charge region near the upper cloud boundary and a vast reservoir of negative charge in a horizontal layer at middle altitudes of the storm, which enabled the discharge to transfer an extraordinary amount of charge between the thundercloud and the ionosphere (300 C).

MATERIALS AND METHODS

VHF lightning mapping array measurements

The VHF lightning mapping array data were from the Oklahoma Lightning Mapping Array (*68*), which has two clusters, one in southwest and one in central Oklahoma, USA. The arrays use time-of-arrival techniques to geolocate VHF pulses (60 to 66 MHz) emitted from lightning. The data were filtered to only include χ^2 values of $\leq$5 for this study. The error ellipses associated with the VHF points for the event are shown in fig. S9, which generally shows small location errors (<1 km) for the sources above the cloud. The charge structure analysis in Fig. 2 was completed by using characteristics inherent to how VHF networks detect leader breakdown in positive or negative charge regions (*14*, *17*, *69*, *70*), such as propagation speeds and VHF power. The VHF speeds are shown in fig. S6. The exponential fit to the VHF points at high altitudes (22 to 45 km) in Fig. 5 is provided by the model $y(x) = ae^{bx} + ce^{dx}$, with a = 23.8, b = 5.4, c = 0.003, and d = 247.2. The fit has an r^2 of 0.85.

Radar and satellite measurements

The radar data for this study are from the Weather Surveillance Radar 88-Doppler network (WSR-88d), which is operated by the National Oceanic Aviation Administration. The radar operates at S band (10 cm). Base reflectivity, which is a measure of the power backscattered to the radar, was used for the analysis to produce Figs. 1 to 3. The specific radar used from the WSR-88d network is located in Frederick, OK (KFDR, latitude = 34.34°N, longitude = 98.98°W). The satellite measurements come from the Advanced Baseline Imager (ABI) and the GLM on the GOES 16 and 17. ABI monitors Earth with 16 spectral bands from the visible to IR with a spatial domain of nearly a hemisphere from GOES 16 and 17 (*71*). The ABI data in Fig. 1A are of the channel 13 (IR) brightness temperature. GLM is a high-speed optical detector that records transient optical pulses at 500 frames per second (2-ms time resolution). The pixel size is 8 km at nadir and 14 km at the edge of its field of view and observes the 777.4 nm (OI) emission line during both night and day (*48*). GLM detections are organized into event, group, and flash features that describe the recorded lightning signals on temporal and spatial scales ranging from 1 pixel within 2 ms to tens to hundreds of pixels over multiple seconds (*72*). Events are the smallest unit of detection and are defined as a single pixel detected above a dynamic threshold. Groups describe one or more events that occur in adjacent pixels in the same 2 ms frame and, when plotted, can map out the structure of a lightning flash (*73*, *74*). Groups that are close in space and time to one another are clustered into features that describe individual flashes. The analysis for this manuscript used group data from GLM.

GLM altitude calculations

The GLM altitude calculation takes pairs of GLM 16 and GLM 17 groups that occur close to each other in space and time (for proper correlation) and uses a least squares technique based on the look vectors from the individual instruments to the group amplitude-weighted centroids to determine a 3D location of the combined group. The technique is described in detail in (*38*). The spatial and temporal constraints used for our study were 90 km and 3 ms. A larger spatial constraint was used when compared to (*38*) to allow for detection of high-altitude GLM sources (higher altitude equals larger separation between correlated GLM 16/17 group pairs). The procedures are as follows:

1) Determine GLM 16 and GLM 17 group pairs from the two orbital detectors.

2) Calculate the initial group 3D locations determined by the two sensors, which use a model lightning ellipsoid for the altitude that ranges from 6 km above sea level at the poles to 14 km at the equator (*75*).

3) Determine the initial two look vectors from the individual GLMs to the initial locations of the lightning groups.

4) Create a grid in the vicinity of the two lightning group locations.

5) Determine the look vectors from each GLM to all grid points.

6) Find the 3D location in the grid that minimizes the sum of squares differences between the final look vectors and the initial nominal look vectors.

The location uncertainty for the 3D GLM sources is 5.2 km in the horizontal direction and 4 km in the vertical direction. Figure S12 shows the associated vertical standard errors plotted with the VHF data as a function of time. The uncertainties are calculated according to section 5 of (*38*). An animation of the group evolution for each GLM is shown in movie S3, with supporting text describing the video in S5 and S6 in the Supplementary Materials.

Magnetic field measurements

The magnetic field measurements came from instruments located at Duke University and the island of Sal of Cape Verde (*27*) that record magnetic field transients from ELF to very low frequency bands (2 to 25 kHz). By using the azimuthal magnetic field, the current moment and the time-integrated charge moment were calculated by techniques previously established for gigantic jet lightning (*5*). The waveforms in figs. S4 and S5 have been corrected for the propagation delay between the instrument and the event.

SUPPLEMENTARY MATERIALS

Supplementary material for this article is available at https://science.org/doi/10.1126/sciadv.abl8731

REFERENCES AND NOTES

1. W. A. Lyons, T. E. Nelson, R. A. Armstrong, V. P. Pasko, M. A. Stanley, Upward electrical discharges from thunderstorm tops. *Bull. Am. Meteorol. Soc.* **84**, 445–454 (2003).
2. V. P. Pasko, Recent advances in theory of transient luminous events. *J. Geophys. Res.* **115**, A00E35 (2010).
3. N. Y. Liu, M. G. McHarg, H. C. Stenbaek-Nielsen, High-altitude electrical discharges associated with thunderstorms and lightning. *J. Atmos. Solar Terr. Phys.* **136**, 98–118 (2015).
4. A. B. Chen, C.-L. Kuo, Y.-J. Lee, H.-T. Su, R.-R. Hsu, J.-L. Chern, H. U. Frey, S. B. Mende, Y. Takahashi, H. Fukunishi, Y.-S. Chang, T.-Y. Liu, L.-C. Lee, Global distributions and occurrence rates of transient luminous events. *J. Geophys. Res.* **113**, A08306 (2008).
5. S. A. Cummer, J. Li, F. Han, G. Lu, N. Jaugey, W. A. Lyons, T. E. Nelson, Quantification of the troposphere-to-ionosphere charge transfer in a gigantic jet. *Nat. Geosci.* **2**, 617–620 (2009).
6. G. Lu, R. Grandin, C. Lasserre, M.-P. Doin, G. Peltzer, Lightning development associated with two negative gigantic jets. *Geophys. Res. Lett.* **38**, L17311 (2011).
7. N. Y. Liu, N. Spiva, J. R. Dwyer, H. K. Rassoul, D. Free, S.A. Cummer, Upward electrical discharges observed above Tropical Depression Dorian. *Nat. Commun.* **6**, 1–8 (2015).
8. V. P. Pasko, M. A. Stanley, J. D. Matthews, U. S. Inan, T. G. Wood, Electrical discharge from a thundercloud top to the lower ionosphere. *Nature* **416**, 152–154 (2002).
9. H. T. Su, R. R. Hsu, A. B. Chen, Y. C. Wang, W. S. Hsiao, W. C. Lai, L. C. Lee, M. Sato, H. Fukunishi, Gigantic jets between a thundercloud and the ionosphere. *Nature* **423**, 974–976 (2003).
10. S. Soula, O. van der Velde, J. Montanya, P. Huet, C. Barthe, J. Bór, Gigantic jets produced by an isolated tropical thunderstorm near Réunion Island. *J. Geophys. Res. Atmos.* **116**, D19103 (2011).
11. S.-M. Huang, K. M. Johnson, Strain accumulation across strike-slip faults: Investigation of the influence of laterally varying lithospheric properties. *J. Geophys. Res.* **117**, B09407 (2012).
12. T. C. Meyer, T. J. Lang, S. A. Rutledge, W. A. Lyons, S. A. Cummer, G. Lu, D. T. Lindsey, Radar and lightning analyses of gigantic jet-producing storms. *J. Geophys. Res. Atmos.* **118**, 2872–2888 (2013).
13. S. Lazarus, M. Splitt, J. Brownlee, N. Spiva, N. Y. Liu, A thermodynamic, kinematic and microphysical analysis of a jet and gigantic jet-producing Florida thunderstorm. *J. Geophys. Res.* **120**, 8469–8490 (2015).
14. L. D. Boggs, N. Liu, J. A. Riousset, F. Shi, S. Lazarus, M. Splitt, H. K. Rassoul, Thunderstorm charge structures producing gigantic jets. *Sci. Rep.* **8**, 18085 (2018).
15. L. D. Boggs, N. Liu, M. Peterson, S. Lazarus, M. Splitt, F. Lucena, A. Nag, H. K. Rassoul, First observations of gigantic jets from geostationary orbit. *Geophys. Res. Lett.* **46**, 3999–4006 (2019).
16. S. M. Lazarus, J. Chiappa, H. Besing, M. E. Splitt, J. A. Riousset, Distinguishing characteristics of the tropical cyclone gigantic jet environment. *J. Atmos. Sci.* **78**, 2741–2761 (2021).
17. P. R. Krehbiel, J. A. Riousset, V. P. Pasko, R. J. Thomas, W. Rison, M. A. Stanley, H. E. Edens, Upward electrical discharges from thunderstorms. *Nat. Geosci.* **1**, 233 (2008).
18. J. A. Riousset, V. P. Pasko, P. R. Krehbiel, W. Rison, M. A. Stanley, Modeling of thundercloud screening charges: Implications for blue and gigantic jets. *J. Geophys. Res.* **115**, A00E10 (2010).
19. H. J. Christian, R. J. Blakeslee, S. J. Goodman, The detection of lightning from geostationary orbit. *J. Geophys. Res. Atmos.* **94**, 13329 (1989).
20. X. Chang, P. Yuan, J. Cen, X. Wang, Variation of the channel temperature in the transmission of lightning leader. *J. Atmos. Sol. Terr. Phys.* **159**, 41–47 (2017).
21. L. Boggs, "Remote sensing, modeling, and spectroscopic studies of gigantic jets and lightning leaders," Ph.D. thesis, Florida Institute of Technology (2019).
22. J. Harley, L. A. Zimmerman, H. E. Edens, H. C. Stenbaek-Nielsen, R. K. Haaland, R. G. Sonnenfeld, M. G. McHarg, High-speed spectra of a bolt from the blue lightning stepped leader. *J. Geophys. Res. Atmos.* **126**, e2020JD033884 (2021).
23. Y. P. Raizer, in *Gas Discharge Physics* (Springer-Verlag, 1991).

24. E. M. Bazelyan, Y. P. Raizer, in *Lightning Physics and Lightning Protection* (IoP Publishing Ltd, 2000).
25. E. M. Wescott, D. D. Sentman, H. C. Stenbaek-Nielsen, P. Huet, M. J. Heavner, D. R. Moudry, New evidence for the brightness and ionization of blue starters and blue jets. *J. Geophys. Res.* **106**, 21549–21554 (2001).
26. V. P. Pasko, Blue jets and gigantic jets: Transient luminous events between thunderstorm tops and the lower ionosphere. *Plasma Phys. Control. Fusion* **50**, 124050 (2008).
27. O. A. van der Velde, J. Montanyà, J. A. López, S. A. Cummer, Gigantic jet discharges evolve stepwise through the middle atmosphere. *Nat. Commun.* **10**, 4350 (2019).
28. C. L. Kuo, J. K. Chou, L. Y. Tsai, A. B. Chen, H. T. Su, R. R. Hsu, S. A. Cummer, H. U. Frey, S. B. Mende, Y. Takahashi, L. C. Lee, Discharge processes, electric field, and electron energy in ISUAL-recorded gigantic jets. *J. Geophys. Res.* **114** (2009).
29. T. Neubert, O. Chanrion, E. Arnone, F. Zanotti, S. Cummer, J. Li, M. Füllekrug, S. Soula, O. van der Velde, The properties of a gigantic jet reflected in a simultaneous sprite: Observations interpreted by a model. *J. Geophys. Res. Space Phys.* **116**, A12329 (2011).
30. C. L. da Silva, V. P. Pasko, Simulation of leader speeds at gigantic jet altitudes. *Geophys. Res. Lett.* **39**, L13805 (2012).
31. K.-M. Peng, R. R. Hsu, W. Y. Chang, H. T. Su, A. B. C. Chen, J. K. Chou, Y. J. Wu, S. C. Chang, C. L. Hung, I. C. Yang, S. H. Tsai, Triangulation and coupling of gigantic jets near the lower ionosphere altitudes. *J. Geophys. Res. Space Physics* **123**, 6904–6916 (2018).
32. J. A. Riousset, V. P. Pasko, A. Bourdon, Air-density-dependent model for analysis of air heating associated with streamers, leaders, and transient luminous events. *J. Geophys. Res.* **115**, A12321 (2010).
33. P. O. Kochkin, A. P. van Deursen, U. Ebert, Experimental study of the spatio-temporal development of metre-scale negative discharge in air. *J. Phys. D Appl. Phys.* **47**, 145203 (2014).
34. P. Kochkin, N. Lehtinen, A. L. P. van Deursen, N. Østgaard, Pilot system development in metre-scale laboratory discharge. *J. Phys. D Appl. Phys.* **49**, 425203 (2016).
35. I. Gallimberti, G. Bacchiega, A. Bondiou-Clergerie, P. Lalande, Fundamental processes in long air gap discharges. *C. R. Physique* **3**, 1335 (2002).
36. S. A. Cummer, Current moment in sprite-producing lightning. *J. Atmos. Sol.-Terr. Phys.* **65**, 499–508 (2003).
37. G. Lu, S. A. Cummer, J. Li, L. Zigoneanu, W. A. Lyons, M. A. Stanley, W. Rison, P. R. Krehbiel, H. E. Edens, R. J. Thomas, W. H. Beasley, S. A. Weiss, R. J. Blakeslee, E. C. Bruning, D. R. MacGorman, T. C. Meyer, K. Palivec, T. Ashcraft, T. Samaras, Coordinated observations of sprites and in-cloud lightning flash structure. *J. Geophys. Res. Atmos.* **118**, 6607–6632 (2013).
38. D. Mach, K. Virts, A technique for determining three-dimensional storm cloud-top locations using stereo optical lightning pulses observed from orbit. *J. Atmos. Oceanic Tech.* **38**, 1993–2001 (2021).
39. K. Cummins, M. Murphy, An overview of lightning locating systems: History, techniques, and data uses, with an in-depth look at the U.S. NLDN. *IEEE Trans. Electromagn. Compat.* **51**, 499–518 (2009).
40. D. R. Greene, R. A. Clark, Vertically integrated liquid water—A new analysis tool. *Mon. Weather Rev.* **100**, 548–552 (1972).
41. L. D. Boggs, N. Liu, M. Splitt, S. Lazarus, C. Glenn, H. Rassoul, S. A. Cummer, An analysis of five negative sprite-parent discharges and their associated thunderstorm charge structures. *J. Geophys. Res.* **121**, 759–784 (2016).
42. Y. Qi, J. Zhang, P. Zhang, A real-time automated convective and stratiform precipitation segregation algorithm in native radar coordinates. *Q. J. Roy. Meteorol. Soc.* **139**, 2233–2240 (2013).
43. B.-C. Seo, W. F. Krajewski, Y. Qi, Utility of vertically integrated liquid water content for radar-rainfall estimation: Quality control and precipitation type classification. *Atmos. Res.* **236**, 104800 (2020).
44. P. R. Krehbiel, R. J. Thomas, W. Rison, T. Hamlin, J. Harlin, M. Davis, GPS-based mapping system reveals lightning inside storms. *Eos, Trans. Am. Geophys. Union* **81**, 21 (2000).
45. G. Lu, S. A. Cummer, J. Li, F. Han, R. J. Blakeslee, H. J. Christian, Charge transfer and in-cloud structure of large-charge-moment positive lightning strokes in a mesoscale convective system. *Geophys. Res. Lett.* **36**, (2009).
46. T. J. Lang, S. A. Rutledge, K. C. Wiens, Origins of positive cloud-to-ground lightning in the stratiform region of a mesoscale convective system. *Geophys. Res. Lett.* **31**, L10105 (2004).
47. T. J. Lang, W. A. Lyons, S. A. Cummer, B. R. Fuchs, B. Dolan, S. A. Rutledge, P. Krehbiel, W. Rison, M. Stanley, T. Ashcraft, Observations of two sprite-producing storms in Colorado. *J. Geophys. Res. Atmos.* **121**, 9675–9695 (2016).
48. S. J. Goodman, R. J. Blakeslee, W. J. Koshak, D. Mach, J. Bailey, D. Buechler, L. Carey, C. Schultz, M. Bateman, E. McCaul Jr., G. Stano, The GOES-R geostationary lightning mapper (GLM). *Atmos. Res.* **125**, 34–49 (2013).
49. T. A. Warner, R. E. Orville, J. L. Marshall, K. Huggins, Spectral (600–1050 nm) time exposures (99.6 μ s) of a lightning stepped leader. *J. Geophys. Res. Atmos.* **116**, 12210 (2011).
50. T. D. Walker, H. J. Christian, Triggered lightning spectroscopy: Part 1. A qualitative analysis. *J. Geophys. Res. Atmos.* **122**, 8000–8011 (2017).
51. L. D. Boggs, N. Liu, A. Nag, T. D. Walker, H. J. Christian, C. L. da Silva, M. Austin, F. Aguirre, H. K. Rassoul, Vertical temperature profile of natural lightning return strokes derived from optical spectra. *J. Geophys. Res. Atmos.* **126**, e2020JD034438 (2021).
52. J. Cen, P. Yuan, S. Xue, X. Wang, Spectral characteristics of lightning dart leader propagating in long path. *Atmos. Res.* **164–165**, 95–98 (2015).
53. J. C. Smith, R. L. Morris, C. Rumpf, R. Longenbaugh, N. McCurdy, C. Henze, J. Dotson, An automated bolide detection pipeline for GOES GLM. *Icarus* **368**, 114576 (2021).
54. J. N. Tilles, P. R. Krehbiel, M. A. Stanley, W. Rison, N. Liu, F. Lyu, S. A. Cummer, J. R. Dwyer, S. Senay, H. Edens, X. Fan, R. G. Brown, J. Wilson, Radio interferometer observations of an energetic in-cloud pulse reveal large currents generated by relativistic discharges. *J. Geophys. Res. Atmos.* **125**, e2020JD032603 (2020).
55. T. D. Hamlin, "The new mexico tech lightning mapping array," thesis, New Mexico Institute of Mining and Technology Socorro (2004).
56. T. C. Marshall, M. Stolzenburg, C. R. Maggio, L. M. Coleman, P. R. Krehbiel, T. Hamlin, R. J. Thomas, W. Rison, Observed electric fields associated with lightning initiation. *Geophys. Res. Lett.* **32**, L03813 (2005).
57. W. D. Rust, D. R. MacGorman, E. C. Bruning, S. A. Weiss, P. R. Krehbiel, R. J. Thomas, W. Rison, T. Hamlin, J. Harlin, Inverted-polarity electrical structures in thunderstorms in the Severe Thunderstorm Electrification and Precipitation Study (STEPS). *Atmos. Res.* **76**, 247–271 (2005).
58. M. Stolzenburg, T. C. Marshall, Charge structure and dynamics in thunderstorms, in *Planetary Atmospheric Electricity*, F. Leblanc, K. L. Aplin, Y. Yair, R. G. Harrison, J. Pl. Lebreton, M. Blanc, Eds. (Springer, 2008), pp. 355.
59. J. E. Dye, A. Bansemer, Electrification in mesoscale updrafts of deep stratiform and anvil clouds in Florida. *J. Geophys. Res. Atmos.* **124**, 1021–1049 (2019).
60. O. A. Van Der Velde, J. Bór, J. Li, S. A. Cummer, E. Arnone, F. Zanotti, M. Füllekrug, C. Haldoupis, S. N. Amor, T. Farges, Multi-instrumental observations of a positive gigantic jet produced by a winter thunderstorm in Europe. *J. Geophys. Res. Atmos.* **115**, D24301 (2010).
61. T. Neubert, O. Chanrion, M. Heumesser, K. Dimitriadou, L. Husbjerg, I. L. Rasmussen, N. Østgaard, V. Reglero, Observation of the onset of a blue jet into the stratosphere. *Nature* **589**, 371–375 (2021).
62. J. Yang, X. Qie, L. Zhong, Q. He, G. Lu, Z. Wang, Y. Wang, N. Liu, F. Liu, K.-M. Peng, B. Zhu, A. Huang, M. Sato, H. Pan, H. Li, Analysis of a gigantic jet in Southern China: Morphology, meteorology, storm evolution, lightning, and narrow bipolar events. *J. Geophys. Res. Atmos.* **125**, e2019JD031538 (2020).
63. C. L. da Silva, V. P. Pasko, Vertical structuring of gigantic jets. *Geophys. Res. Lett.* **40**, 3315–3319 (2013).
64. C. L. da Silva, V. P. Pasko, Dynamics of streamer-to-leader transition at reduced air densities and its implications for propagation of lightning leaders and gigantic jets. *J. Geophys. Res.* **118**, 13,561–13,590 (2013a).
65. Y. P. Raizer, G. M. Milikh, M. N. Shneider, On the mechanism of blue jet formation and propagation. *Geophys. Res. Lett.* **33**, L23801 (2006).
66. A. E. Hedin, Extension of the MSIS Thermosphere Model into the middle and lower atmosphere. *J. Geophys. Res. Space Physics* **96**, 1159–1172 (1991).
67. F. Shi, N. Liu, J. R. Dwyer, K. M. Ihaddadene, VHF and UHF electromagnetic radiation produced by streamers in lightning. *Geophys. Res. Lett.* **46**, 443–451 (2019).
68. R. J. Thomas, E. J. Garnero, T. Lay, High-resolution imaging of lowermost mantle structure under the Cocos plate. *J. Geophys. Res.* **109**, B08307 (2004).
69. R. J. Thomas, P. R. Krehbiel, W. Rison, T. Hamlin, J. Harlin, D. Shown, Observations of vhf source powers radiated by lightning. *Geophys. Res. Lett.* **28**, 143–146 (2001).
70. K. C. Wiens, S. A. Rutledge, S. A. Tessendorf, The 29 June 2000 Supercell Observed during STEPS. Part II: Lightning and Charge Structure. *J. Atmos. Sci.* **62**, 4151–4177 (2005).
71. T. J. Schmit, P. Griffith, M. M. Gunshor, J. M. Daniels, S. J. Goodman, W. J. Lebair, A closer look at the ABI on the GOES-R series. *Bull. Am. Meteorol. Soc.* **98**, 681–698 (2017).
72. D. M. Mach, Geostationary lightning mapper clustering algorithm stability. *J. Geophys. Res. Atmos.* **125**, e2019JD031900 (2020).
73. M. Peterson, S. Rudlosky, W. Deierling, The properties of optical lightning flashes and the clouds they illuminate. *J. Geophys. Res. Atmos.* **122**, 423–442 (2017).
74. M. Peterson, S. Rudlosky, W. Deierling, Mapping the lateral development of lightning flashes from orbit. *J. Geophys. Res. Atmos.* **123**, 9674–9687 (2018).
75. K. S. Virts, W. J. Koshak, Mitigation of geostationary lightning mapper geolocation errors. *J. Atmos. Oceanic Tech.* **37**, 1725–1736 (2020).

Acknowledgments: We would like to thank F. Lucena for information about the gigantic jet captured in fig. S1. We would also like to thank the pilot who captured it, C. Holmes, for additional information and permission to publish the images of the event. **Funding:** This work was, in part, supported by NASA grant 80MSFC17M0022 and NNX17AJ10G, the U.S. and European Geostationary Lightning Sensor Cross-Validation Study, and AFOSR grant no. FA9550-18-1-0358 to the University of New Hampshire. O.A.v.d.V. and J.M. are

supported by grant PID2019-109269RB-C42 funded by MCIN/AEI/10.13039/501100011033.
Author contributions: L.D.B., E.B., N.L., D.MacG., and O.v.d.V. analyzed the VHF lightning mapping array data and radar data to understand the thunderstorm charge structure of the event. L.D.B., E.B., V.C., and D.MacG. analyzed the radar and satellite data to understand the meteorology of the event. D. Mach, M.P., and L.D.B. analyzed the Geostationary Lightning Mapper data. O.v.d.V., J.M., and S.C. analyzed and interpreted the extremely low frequency sferic data. All authors contributed to the discussion of the results and preparation of the manuscript. **Competing interests:** The authors declare that they have no competing interests.

Data and materials availability: The data used in the analysis of this manuscript can be found at https://figshare.com/projects/Gigantic_Jet_OK_2018/118446. All data needed to evaluate the conclusions in the paper are present in the paper and/or the Supplementary Materials.

Submitted 10 August 2021
Accepted 21 June 2022
Published 3 August 2022
10.1126/sciadv.abl8731